IEEE Access
Multidisciplinary | Rapid Review | Open Access Journal

Received May 3, 2022, accepted May 27, 2022, date of publication May 30, 2022, date of current version June 9, 2022.

Digital Object Identifier 10.1109/ACCESS.2022.3179360

Z-Shaped Metasurface-Based Wideband Circularly Polarized Fabry–Pérot Antenna for C-Band Satellite Technology

NATHAPAT SUPREEYATITIKUL[1], AKKARAT BOONPOONGA[2], (Member, IEEE), AND CHUWONG PHONGCHAROENPANICH[1], (Member, IEEE)

[1]School of Engineering, King Mongkut's Institute of Technology Ladkrabang, Bangkok 10520, Thailand
[2]Research Center of Innovation Digital and Electromagnetic Technology, Department of Electrical and Computer Engineering, Faculty of Engineering, King Mongkut's University of Technology North Bangkok, Bangkok 10800, Thailand

Corresponding author: Chuwong Phongcharoenpanich (chuwong.ph@kmitl.ac.th)

This work was supported in part by the National Science, Research and Innovation Fund (NSRF), and in part by the King Mongkut's University of Technology North Bangkok under Contract KMUTNB-FF-65-26.

ABSTRACT This research proposes a low-profile Z-shaped metasurface (MTS)-based wideband circularly polarized (CP) Fabry–Pérot antenna for C-band satellite communication. The proposed low-cost and low-complexity CP Fabry–Pérot antenna is realized by using three substrate layers: upper, middle, and lower. The substrates are of FR-4 type with a dielectric constant of 4.3 and loss tangent of 0.025. The upper substrate contains 9 × 9 periodically-arranged Z-shaped MTS unit cells functioning as the partially reflecting surface and circular polarization conversion, and at the center of the middle substrate sits a corners-truncated square patch. The lower substrate consists of a copper plate with an H-shaped slot at the center of the ground plane and a microstrip feed line. The lower and middle substrates function as the source antenna. The periodic Z-shaped MTS unit cells are utilized to enhance the impedance bandwidth (IBW) and gain of the source antenna and also to convert linearly polarized into CP wave. The antenna dimension is $1.5\lambda_0 \times 1.5\lambda_0 \times 0.51\lambda_0$. Simulations are performed and experiments carried out. The measured IBW and axial ratio bandwidth are 64% (4.4 – 7.6 GHz) and 18% (4.4 – 5.3 GHz) at the center frequency of 5 GHz. In addition, the proposed antenna scheme achieves a measured 3-dB boresight gain bandwidth of 30% (4.3 – 5.8 GHz) with the maximum gain of 12.88 dBic at 4.7 GHz, rendering the proposed Z-shaped MTS-based CP Fabry–Pérot antenna operationally suitable for satellite communication. In essence, the novelty of this research lies in the use of the low-cost and low-complexity Z-shaped MTS unit cell to effectively enhance the antenna gain and convert LP into CP wave.

INDEX TERMS C-band, Fabry–Perot, metasurfaces, satellite communication, wideband.

I. INTRODUCTION

In satellite communication, circularly polarized (CP) patch antennas play an important role in receiving or transmitting signals in various planes. Unlike linearly polarized (LP) antennas, the CP patch antennas are less susceptible to fading or multipath interference. The CP patch antennas nonetheless suffer from low gain due to dielectric loss. To overcome the low gain inherent in the conventional CP patch antennas, several techniques have been proposed and incorporated into the CP antennas, such as CP antenna arrays [1], CP dielectric resonator antenna [2], and CP Fabry–Pérot antenna [3]. Of particular interest are Fabry–Pérot antennas [4], [5] which could achieve higher gain with lower cost and less complexity, vis-à-vis the CP antenna arrays and CP dielectric resonator antenna. A typical Fabry–Pérot antenna consists of an LP source antenna (e.g., microstrip patch, dipole antenna), which is placed with air-gap cavity between the partially reflective surface (PRS) and the fully reflective ground plane.

The PRS is typically fashioned from periodically-arranged metasurface (MTS) elements functioning as the superstrate [6] to covert LP to CP wave [7] and to enhance the antenna gain [8]. The cavity between the PRS and the reflective ground plane affects the resonance characteristics of the antenna [9] and the antenna performance, including

The associate editor coordinating the review of this manuscript and approving it for publication was Weiren Zhu.

the impedance bandwidth (IBW), axial ratio bandwidth (ARBW), gain, and radiation efficiency.

In [10], a single-feed microstrip CP antenna using PRS with 9 × 9 square patch MTS elements as the Fabry–Pérot antenna for C-band spectrum achieves an IBW of 32% (37.4 – 52.2 GHz), 3-dB ARBW of 2.58% (5.725 – 5.875 GHz), and maximum gain of 17.3 dBic at 5.8 GHz. In [11], a single-feed microstrip patch antenna using the PRS superstrate with 5 × 5 tapered rectangular-shaped MTS elements for X-band spectrum achieves an IBW of 20% (8 – 9.8 GHz), 3-dB ARBW of 6.67% (8.35 – 8.95 GHz), and maximum gain of 14.6 dBic at 8.3 GHz. In [12], a CP Fabry–Pérot antenna consisting of a rectangle patch antenna surrounded by thin-rectangular-shaped MTS elements as high impedance surface (on the middle substrate) and of 6 × 6 square-split-ring MTS elements (on the upper substrate) functioning as PRS and CP conversion for X-band spectrum achieves an IBW of 2.61% (10.5 – 10.78 GHz), 3-dB ARBW of 0.84% (10.65 – 10.74 GHz), and maximum gain of 9.8 dBic at 10.7 GHz.

In [13], a CP Fabry–Pérot slot coupled patch antenna using 9 × 9 receiver–transmitter MTS as CP conversion for X-band spectrum achieves an IBW of 4.8% (9.78 – 10.26 GHz), 3-dB ARBW of 4% (9.8 – 10.2 GHz), and maximum gain of 17.8 dBic at 10 GHz. In [14], a Fabry–Pérot antenna with magneto-electric dipole as the source antenna and the PRS with 8 × 8 circular patch MTS elements as CP conversion for Ku-band spectrum achieves an IBW of 54% (11.7 – 19.8 GHz), 3-dB ARBW of 29.3% (12.4 – 16.8 GHz), and maximum gain of 11.45 dBic at 14 GHz. In [15], a dual-feed CP Fabry–Pérot antenna with three-layer sandwiched 10 × 10 MTS elements as CP conversion for X-band spectrum achieves an IBW of 2.8% (9.86 – 10.14 GHz), 3-dB ARBW of 5% (9.75 – 10.25 GHz), and maximum gain of 13.4 dBic at 10 GHz.

In [16], a CP Fabry–Pérot patch array antenna with Wilkinson divider feed network using four-cluster L-shaped MTS elements as PRS and CP conversion for X-/Ku-band spectra achieves an IBW of 30% (9.5 – 12.8 GHz), 3-dB ARBW of 11.6% (9.5 – 13 GHz), and maximum gain of 13.4 dBic at 11 GHz. In [17], a CP slot antenna array with sequentially-rotated feed network using four-cluster MTS elements as the Fabry–Pérot antenna for X-band spectrum achieves an IBW of 13.88% (8.25 – 9.5 GHz), 3-dB ARBW of 21.11% (8.1 – 10 GHz), and maximum gain of 11.2 dBic at 9.2 GHz. However, the CP Fabry–Pérot antennas in [10]–[13] suffer from narrow IBW and ARBW, while those in [14], [15] is very bulky despite high gain. Meanwhile, in spite of wide ARBW, the feed networks of the CP Fabry–Pérot antennas in [16], [17] are very complex.

As a result, this research proposes a compact Z-shaped MTS-based wideband CP Fabry–Pérot antenna for C-band satellite communication system. The proposed antenna is realized using three layers of substrates: upper, middle, and lower, with air gaps between substrates. The upper substrate contains 9 × 9 periodically-arranged Z-shaped MTS unit cells which function as the PRS to enhance the antenna gain and bandwidth. At the center of the middle substrate sits a corners-truncated square patch, and the lower substrate consists of the H-shaped slot ground plane and a microstrip feed line. The lower and middle substrates function as the source antenna. Simulations are performed to optimize the antenna parameters using CST Studio Suite, and an antenna prototype is fabricated and experiments carried out in an anechoic chamber. In this research, the performance metrics of the proposed antenna include the IBW, ARBW, gain, radiation pattern, and radiation efficiency.

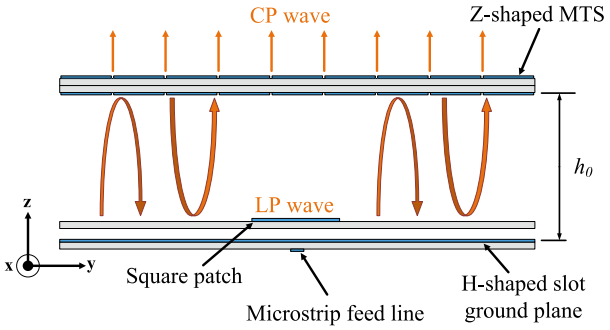

FIGURE 1. Schematic view of the proposed Z-shaped MTS-based CP Fabry–Pérot antenna.

II. ANTENNA DESIGN PROCESS

A. Z-SHAPED MTS ELEMENT DESIGN

Figure 1 illustrates the schematic view of the Z-shaped MTS-based CP Fabry–Pérot antenna. The proposed antenna consists primarily of the Z-shaped MTS (functioning as the partially reflective surface), square patch (functioning as the radiating patch), and H-shaped slot ground plane. The radiating patch on the middle substrate radiates electromagnetic (EM) waves to the partially reflective surface (PRS) on the upper substrate, while some of the EM waves are reflected back by the ground plane (on the lower substrate) into the cavity.

The height of the cavity (h_0) is approximated at half wavelength at the center frequency (5 GHz) [18], [19], which is approximately 33 mm. To derive the cavity height with wide IBW and high gain, optimization was carried out for the optimal cavity height whereby h_0 was varied between 33, 34, and 35 mm. The optimal h_0 is 34 mm, which corresponds to the surface wave resonance.

In addition, to achieve wide 3-dB boresight gain bandwidth, the reflection phase of PRS must be positive. The directivity of the MTS-based Fabry–Pérot antenna is enhanced by PRS whose directivity can be calculated by using equation (1) [20].

$$D = 10 \log \left(\frac{1 + R}{1 - R} \right) \tag{1}$$

where D is the directivity of the antenna and R is the magnitude of reflection coefficient of PRS.

The evolution of the Z-shaped MTS unit cell involves two stages: the MTS unit cell of square shape and the MTS unit cell of Z-character shape, as shown in Figure 2. The upper substrate to which the Z-shaped MTS unit cells are affixed is realized by stacking one substrate (upper-stack substrate) on top of the other substrate (lower-stack substrate) without air gap. Both upper- and lower-stack substrates are of FR-4 with 12 mm × 12 mm ($p \times p$) in dimension ($0.174\lambda_0 \times 0.174\lambda_0$) and 1.6 mm in thickness for h_{t1} and h_{t2}. The dielectric constant (ε_r) and loss tangent ($tan\ \delta$) are 4.3 and 0.025.

Figure 2(a) shows the square-shaped MTS unit cell on the upper substrate layer of the proposed antenna scheme, consisting of the square-shaped element (W_u) on the upper-stack substrate and the square-shaped ground plane (W_l) on the lower-stack substrate. Figure 2(b) shows the simulated model of the square-shaped MTS unit cell. The square-shaped ground plane on the lower-stack substrate receives the incident LP wave from the source antenna (*port 1*) and transmits to the square-shaped element on the upper-stack substrate where the wave is radiated into free space (*port 2*).

However, the square-shaped MTS unit cell possesses low reflectivity and high transmittivity, rendering it less ideal for the PRS due to the resulting low gain. As a result, the square-shaped MTS unit cell is transformed into the Z-shaped MTS unit cell with high reflectivity and low transmittivity.

Figure 2(c) shows the proposed Z-shaped MTS unit cell, consisting of the Z-shaped element and the square-shaped ground plane. The Z-shaped element has evolved from the square-shaped element, while the square-shaped ground plane and the upper- and lower-stack substrates remain unchanged. The function of the Z-shaped MTS unit cell is to convert LP to CP wave.

In the simulation, the boundary condition [21] of the Z-shaped MTS unit cell for x- and y-polarization is of periodic boundaries for xz- and yz-plane, while the Floquet ports (*port 1* and *port 2*) are excited in the z-direction.

Figures 3(a)-(b) show the equivalent circuit models of *x*- and *y*-polarized electric fields, respectively [22]. The Z-shaped element, voids on either side of Z-shaped element, the coupling between the Z-shaped element and the square-shaped ground plane, and square-shaped ground plane serve as the inductor (L_1), series capacitor (C_1 and C_2), parallel capacitor (C_3), series inductor (L_2) and series capacitor (C_4) of the *x*- and *y*-polarized electric fields.

Figures 4(a)-(b) show the magnitude of the simulated reflection coefficient (S_{11}) and transmission coefficient (S_{21}) under variable width of the square-shaped element and the square-shaped ground plane ($W_u = W_l$): 10, 11, and 12 mm. In Figure 4(a), with $W_u = W_l = 10$ and 11 mm, the magnitudes of S_{11} are 0.14 and 0.1 at 5 GHz and 5.77 GHz, respectively. With $W_u = W_l = 12$ mm, the magnitude of S_{11} approaches 1. In Figure 4(b), with $W_u = W_l = 10$ and 11 mm, the magnitudes of S_{21} are 0.86 and 0.88 at 5 GHz and 5.77 GHz, respectively. With $W_u = W_l = 12$ mm,

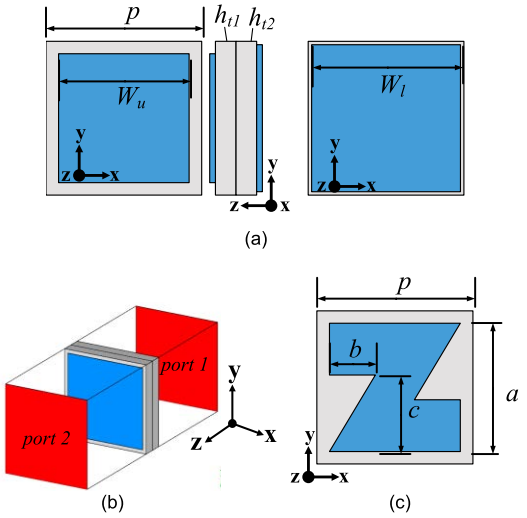

FIGURE 2. Evolution of the Z-shaped MTS unit cell: (a) square-shaped MTS unit cell, (b) simulated model of square-shaped MTS unit cell, (c) Z-shaped MTS unit cell.

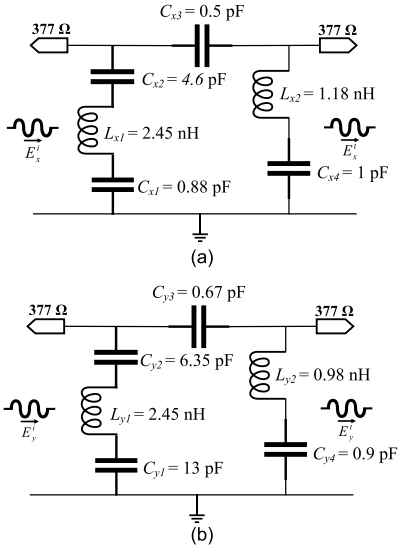

FIGURE 3. Equivalent circuit models of the Z-shaped MTS unit cell: (a) *x*-polarized, (b) *y*-polarization.

the magnitude of S_{21} is close to 0. With $W_u = W_l = 11$, the magnitude of S_{11} of the square-shaped element with the square-shaped ground plane is the lowest around the center frequency of 5 GHz, and the corresponding magnitude of S_{21} peaks in the vicinity of 5 GHz. The optimal W_l is thus 11 mm. However, the square-shaped MTS unit cell possesses low reflectivity and high transmittivity, rendering it less ideal for the PRS due to the resulting low gain.

Figures 5(a)-(b) show the magnitude of the simulated S_{11} and S_{21} under variable width of the square-shaped element (W_u): 9, 10, and 11 mm. As W_u increases, the magnitudes of S_{11} and S_{21} shift to low frequency. With $W_u = 10$ mm, the magnitudes of S_{11} and S_{21} are 0.56 and 0.48 at 5 GHz, achieving high reflectivity and low transmittivity. The optimal W_u is thus 10 mm.

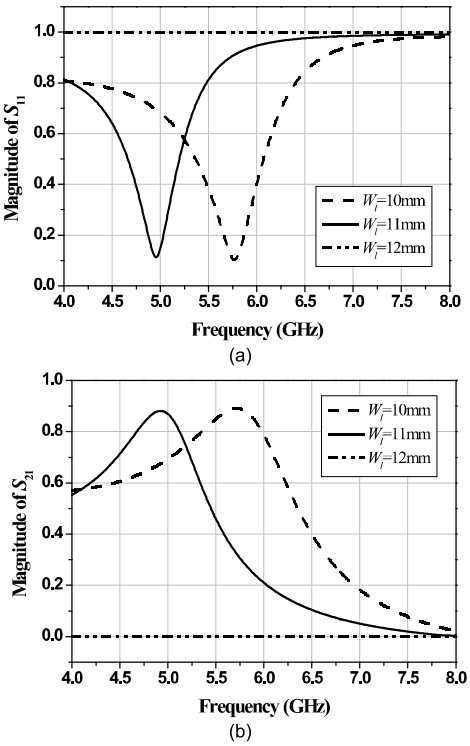

FIGURE 4. Simulated results of the square-shaped ground plane under variable W_l: (a) magnitude of S_{11}, (b) magnitude of S_{21}.

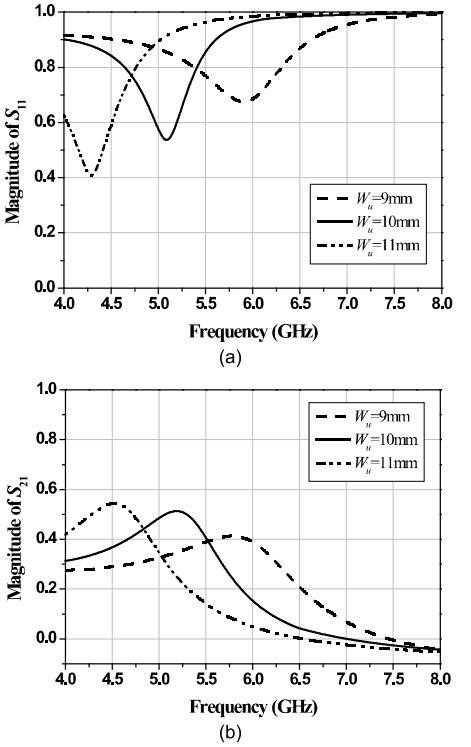

FIGURE 5. Simulated results of the square-shaped MTS element under variable W_u: (a) magnitude of S_{11}, (b) magnitude of S_{21}.

To realize the LP-to-CP conversion for the Z-shaped MTS unit cell, the magnitude of S_{21} of x- and y-polarization waves at the center frequency of 5 GHz must be identical ($T_x = T_y$), and the corresponding phase difference between the magnitude of S_{21} of x- and y-polarization waves ($\phi_{Tx} - \phi_{Ty}$) is equal to $\pm 90°$. The CP wave is characterized by the axial ratio (AR) which can be calculated by equation (2), as shown at the bottom of the page, [23]. where T_x and T_y are the transmission coefficients of the x- and y-polarization waves, respectively, and $\Delta\phi$ is the phase difference between the x- and y-polarization waves.

Figures 6(a)-(b) show the magnitude and phase of S_{21} under variable b: 2.5, 3.5, and 4.5 mm (refer to Figure 2). In Figure 6(a), the magnitudes of S_{21} associated with the x- and y-polarization (x- and y-pol) waves for $b = 2.5$, 3.5, and 4.5 mm are identical: 0.57, 0.48, and 0.43 at 5.2, 5.06, and 4.7 GHz, respectively. In Figure 6(b), as b increased (2.5, 3.5, and 4.5 mm), the phase difference of the magnitude of S_{21} between x- and y-pol waves at 5 GHz are 44°, 88°, and 121°, respectively. Given $b = 3.5$ mm, the phase difference of the magnitude of S_{21} between x- and y-pol waves at 5 GHz is 88°. The optimal b is 3.5 mm.

Figures 7(a)-(b) show the magnitude and phase of S_{21} under variable c: 5, 6, and 7 mm (refer to Figure 2). In Figure 7(a), as c increases, the magnitudes of S_{21} associated with the x- and y-pol waves for $c = 5$, 6, and 7 mm are identical: 0.52, 0.49, and 0.46 at 5.15, 5, and 4.85 GHz, respectively. In Figure 7(b), as c increased (5, 6, and 7 mm), the phase difference of the magnitude of S_{21} between x- and y-pol waves at 5 GHz are 59°, 89°, and 119°, respectively. Specifically, with $c = 6$ mm, the phase difference of the magnitude of S_{21} between x- and y-pol waves at 5 GHz is 89°. The optimal c is 6 mm. Specifically, the vertical length (a), the length of the MTS element with voids (p), and the square-shaped ground plane (W_l) of one unit of Z-shaped MTS unit cell are 10, 12, and 11 mm, respectively.

The polarization conversion ratio (PCR) of the proposed Z-shaped MTS unit cell is determined by the reflection coefficients of the co- and cross-polarization waves, as expressed in equation (3) [24].

$$PCR = \frac{R_{LHCP}^2}{R_{LHCP}^2 + R_{RHCP}^2} \tag{3}$$

$$AR = \left(\frac{|T_x|^2 + |T_y|^2 + \sqrt{|T_x|^4 + |T_y|^4 + 2|T_x|^2 |T_y|^2 cos(2\Delta\phi)}}{|T_x|^2 + |T_y|^2 - \sqrt{|T_x|^4 + |T_y|^4 + 2|T_x|^2 |T_y|^2 cos(2\Delta\phi)}} \right)^{1/2} \tag{2}$$

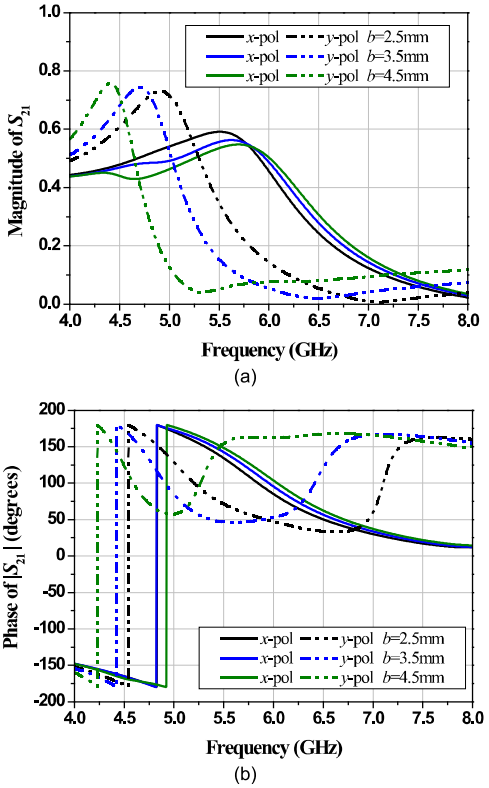

FIGURE 6. Simulated results of the Z-shaped MTS unit cell under variable *b*: (a) magnitude of S_{21}, (b) phase of S_{21}.

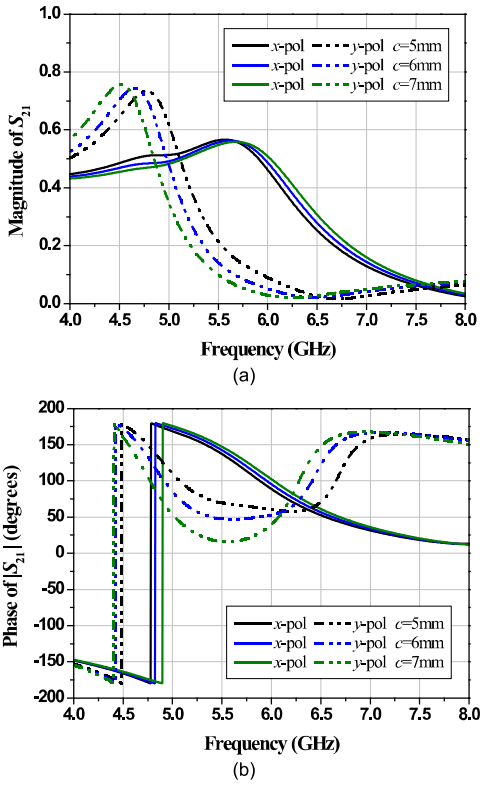

FIGURE 7. Simulated results of the Z-shaped MTS unit cell under variable *c*: (a) magnitude of S_{21}, (b) phase of S_{21}.

where R_{RHCP} and R_{LHCP} are the reflection coefficients of the co- and cross-polarization waves, respectively.

Figure 8(a) shows the reflection coefficients of the co- and cross-polarization waves and the PCR of the Z-shaped MTS unit cell. The simulated reflection coefficient of co-polarization is below −10 dB between 3.6 – 6 GHz, while the simulated reflection coefficient of cross-polarization is above −5 dB between 4.1 – 5.9 GHz. The PCR is greater than 0.9 between 4.3 – 5.2 GHz.

The circular polarization conversion of the Z-shaped MTS unit cell is characterized by the ellipticity (η), which is calculated by equations (4) – (6) [25], [26], respectively.

$$C_+ = E_x^i T_x - jE_y^i T_y \tag{4}$$

$$C_- = E_x^i T_x + jE_y^i T_y \tag{5}$$

$$\eta = tan^{-1}\left(\frac{|C_+| - |C_-|}{|C_+| + |C_-|}\right) \tag{6}$$

where C_+ and C_- are the circular conversion coefficients for left-hand circular polarization (LHCP) and right-hand circular polarization (RHCP), respectively. T_x and T_y are the transmission coefficients of E_x^i and E_y^i [27].

In Figure 8(b), the ellipticity of the Z-shaped MTS unit cell is 40° – 45° between 4.4 – 5.25 GHz for circular polarization. Figures 8(c)-(d) show the azimuth polarization and elliptical polarizations of the Z-shaped MTS unit cell at different frequencies. In Figure 8(c), the azimuth polarization (ψ) is the angle between the major axis of the ellipse and the x-axis relative to the frequency, which can be calculated by equation (7) [28].

$$\psi = (\angle C_+ - \angle C_-)/2 \tag{7}$$

In Figure 8(d), the elliptical polarizations at six frequencies (4, 4.4, 4.8, 5.2, 5.6, and 6 GHz), which correspond to ψ = 87°, 70°, 30°, 20°, 12°, and 8°, respectively, indicating the right-hand polarization.

B. THE Z-SHAPED MTS CP FABRY-PÉROT ANTENNA DESIGN

Figures 9(a)-(c) respectively illustrate the upper, middle, and lower substrate layers of the Z-shaped MTS-based CP Fabry–Pérot antenna for C-band satellite technology. The three substrate layers are of FR-4 type of 108 mm × 108 mm ($W_{sub} \times L_{sub}$) in dimension ($1.5\lambda_0 \times 1.5\lambda_0$) and with air gaps between substrates. The thickness of the upper (h_1), middle (h_2), and lower (h_3) substrates are 3.2 mm, 1.6 mm, and 1.6 mm. The heights of the air gap between the upper and middle substrates (h_{g1}) and between the middle and lower substrates (h_{g2}) are 29.4 mm and 3 mm.

The upper substrate contains 9 × 9 periodic Z-shaped MTS unit cells, and at the center of the middle substrate sits a corners-truncated square patch functioning as the radiating patch. The dimensions of the square patch and truncated corners are 20 mm × 20 mm ($W_p \times L_p$) and 7.5 mm (L_c). Meanwhile, the lower substrate consists of a

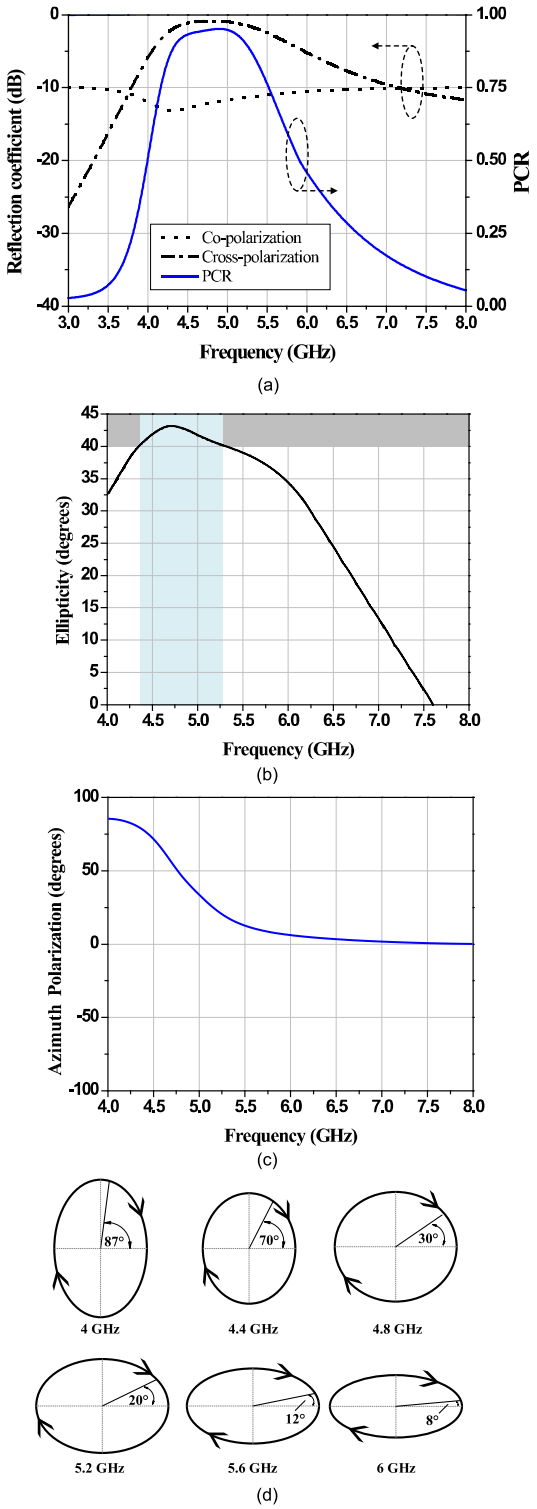

FIGURE 8. Simulated results of the Z-shaped MTS unit cell: (a) reflection coefficient and PCR, (b) ellipticity, (c) azimuth polarization, (d) elliptical polarizations at different frequencies.

microstrip feed line functioning as the signal input and the H-shaped slot at the center of the ground plane (i.e., the aperture-coupled microstrip patch antenna). A conventional rectangular-shaped slot is normally utilized to manipulate the input impedance to achieve the maximum coupling between the radiating patch and ground plane, giving rise to wide IBW [29]. Likewise, the input impedance could be manipulated by varying the slot shape, size, and position. In [30], an H-shaped slot is used to improve the coupling between the radiating patch and ground plane. Meanwhile, the effects of H-shaped slot parameters on the antenna performance are detailed in [31]. The lower and middle substrates function as the source antenna.

The microstrip feed line is 3 mm × 60 mm ($W_f \times L_f$) in dimension, while the dimensions of the H-shaped slot are 2 mm × 20 mm ($W_{S1} \times L_{S1}$) and 4.5 mm × 8 mm ($W_{S2} \times L_{S2}$). The overall dimension of the proposed Z-shaped MTS-based CP Fabry–Pérot antenna is 108 mm × 108 mm × 38.8 mm ($1.5\lambda_0 \times 1.5\lambda_0 \times 0.51\lambda_0$, where λ_0 is the free-space wavelength corresponding to the lowest operating frequency).

Figures 10(a)-(b) show the simulated IBW ($|S_{11}| \leq -10$ dB), ARBW (AR $\leq$ 3 dB), and gain of the source antenna (i.e., the lower and middle substrate layers). The IBW of the source antenna is 62.5% (4.16 – 7.42 GHz), falling within the C-band frequency with the maximum gain of 6.24 dBic at 4.4 GHz. However, the AR of the source antenna is greater than 3 dB (AR > 3 dB). Although the corners-truncated square patch antenna generated the CP wave radiation, the ARBW of the source antenna is greater than 3 dB (failing to achieve CP radiation) as a result of the H-shaped slot in the ground plane. To realize the CP radiation, the Z-shaped MTS elements (i.e., PRS) are incorporated into the proposed antenna scheme.

Figures 11(a)-(c) show the simulated IBW ($|S_{11}| \leq -10$ dB), gain, and ARBW (AR $\leq$ 3 dB) under variable cavity heights (h_0): 33, 34, and 35 mm. In Figure 11(a), as h_0 increases, the IBW becomes slightly wider at lower frequency. Similar to the IBW, the maximum gain also shifts to lower frequency due to improved impedance matching, as shown in Figure 11(b). In Figure 11(c), given equation (1), the height of the cavity (h_0) is approximately $\lambda_0/2$ (33 mm). However, with $h_0 =$ 33 mm, ARBW is narrow (10%), covering 4.5 – 5 GHz. As a result, h_0 is varied to realize wider ARBW. With $h_0 =$ 35 mm, ARBW is 11%, covering 4.7 – 5.25 GHz. Meanwhile, with $h_0 = 34$ mm, ARBW becomes wider (17.4%), covering 4.4 – 5.27 GHz. As a result, the optimal h_0 is 34 mm.

Figures 12(a)-(c) show the simulated IBW ($|S_{11}| \leq -10$ dB), gain, and ARBW (AR $\leq$ 3 dB) under variable numbers of the Z-shaped MTS unit cells on the upper-stack substrate: 7 × 7, 9 × 9, and 11 × 11 unit cells.

In Figure 12(a), given 7 × 7 and 9 × 9 unit cells, the IBW are almost identical and fall between 4.44 – 7.48 GHz. With 11 × 11 unit cells, the IBW becomes slightly wider, covering 4.44 – 7.7 GHz. In Figure 12(b), as the number of the Z-shaped MTS unit cells increases, the maximum gain also increases. The ARBW (AR $\leq$ 3 dB) of 7 × 7 and 9 × 9 unit cells are 6%, covering 4.5 – 4.8 GHz; and 17.4%, covering 4.4 – 5.27 GHz, as shown in Figure 12(c). However, with

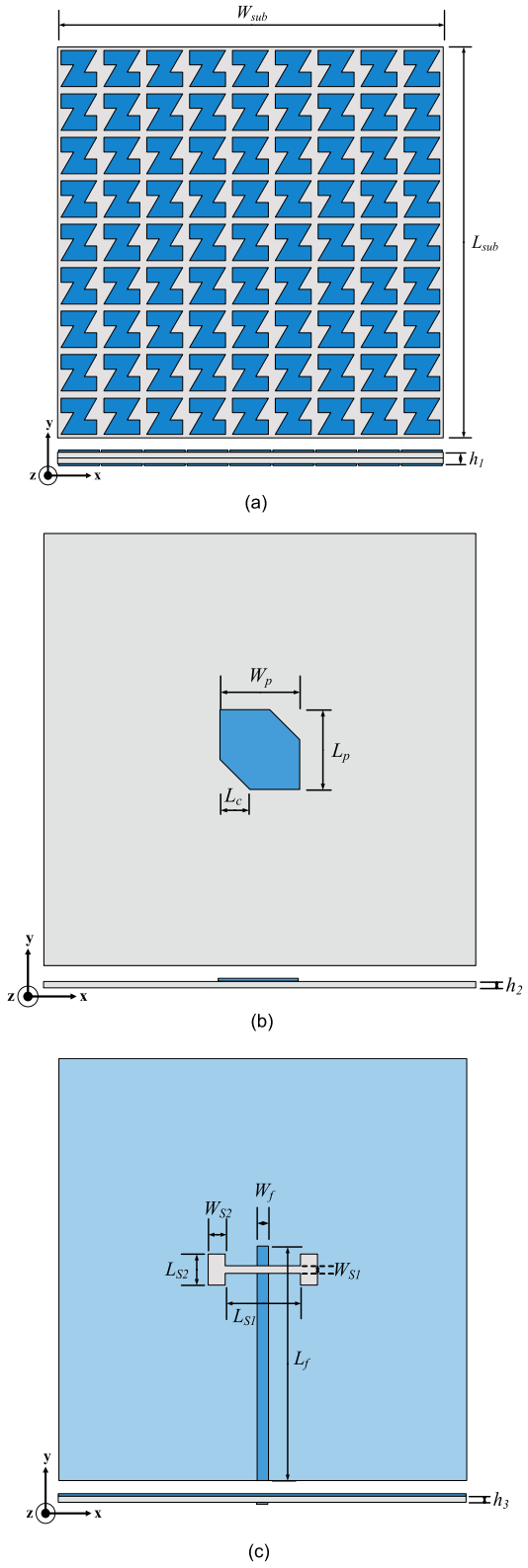

FIGURE 9. Configuration of the Z-shaped MTS-based CP Fabry–Pérot antenna: (a) upper substrate, (b) middle substrate, (c) lower substrate.

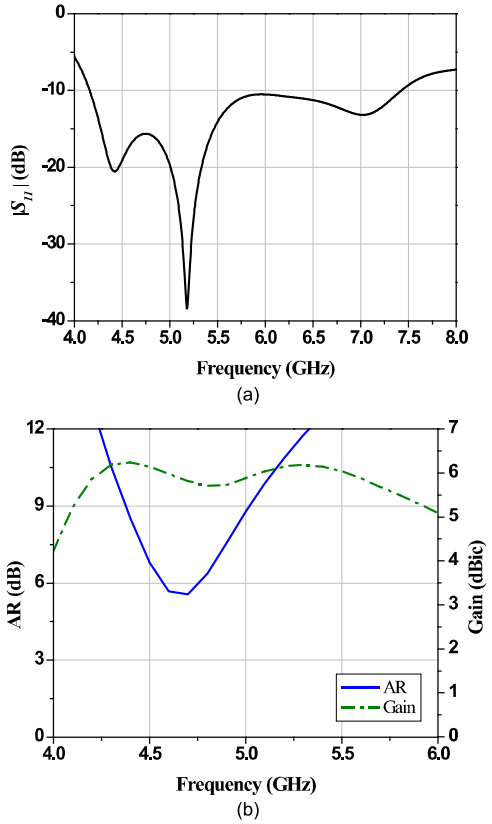

FIGURE 10. Simulated results of the aperture-coupled microstrip patch antenna: (a) IBW, (b) AR and gain.

11×11 unit cells, the ARBW is greater than 3 dB (AR $>$ 3 dB) at 5 GHz. The optimal number of the Z-shaped MTS unit cells is thus 9×9 unit cells. Table 1 tabulates the parameters and optimal dimensions of the Z-shaped MTS-based CP Fabry–Pérot antenna.

The periodic Z-shaped MTS unit cells functioning as the PRS are utilized to enhance the bandwidth of the source antenna. The surface wave resonance [32] of the proposed Z-shaped MTS-based CP Fabry–Pérot antenna propagates on the PRS surface, resulting in high-order resonance mode. In Figure 13(a), the surface wave travels along the length of the PRS corresponding to the resonant length. The surface wave resonance can be calculated by equation (8) [33].

$$\beta_{SW} = \frac{\pi}{W_{sub}} = \frac{\pi}{N \times p} \tag{8}$$

where β_{SW} is the propagation constant of the surface wave resonance, L_{PRS}, N, and p are the length of the PRS, number of the Z-shaped MTS unit cell, and length of the Z-shaped MTS unit cell.

Figure 13(b) is the dispersion diagram of the Z-shaped MTS unit cell. The boundary conditions in the z-direction of the Z-shaped MTS unit cell are the perfect electrical conductor (PEC) in the xz and yz planes for Eigenmode Solver [34]. The resonance modes 1 – 5 are simulated by CST under variable numbers of the Z-shaped MTS unit cells relative to the phase of surface wave.

With $N = 7$ (50.87°) and 9 (39.87°), the resonance mode 4 occurs at 6.7 and 6.2 GHz, respectively, improving the

TABLE 1. Parameters and optimal dimensions of the Z-shaped MTS-based CP Fabry–Pérot antenna.

Parameters	W_{sub}	L_{sub}	h_1	h_2	h_3	h_{t1}	h_{t2}	h_{g1}	h_{g2}
Values (mm)	108	108	3.2	1.6	1.6	1.6	1.6	29.4	3
Parameters	h_0	a	p	b	c	W_a	L_a	W_p	L_p
Values (mm)	34	10	12	3.5	6	11.5	11.5	20	20
Parameters	L_c	W_f	L_f	W_{S1}	LS_1	W_{S2}	L_{S2}		
Values (mm)	7.5	3	60	2	20	4.5	8		

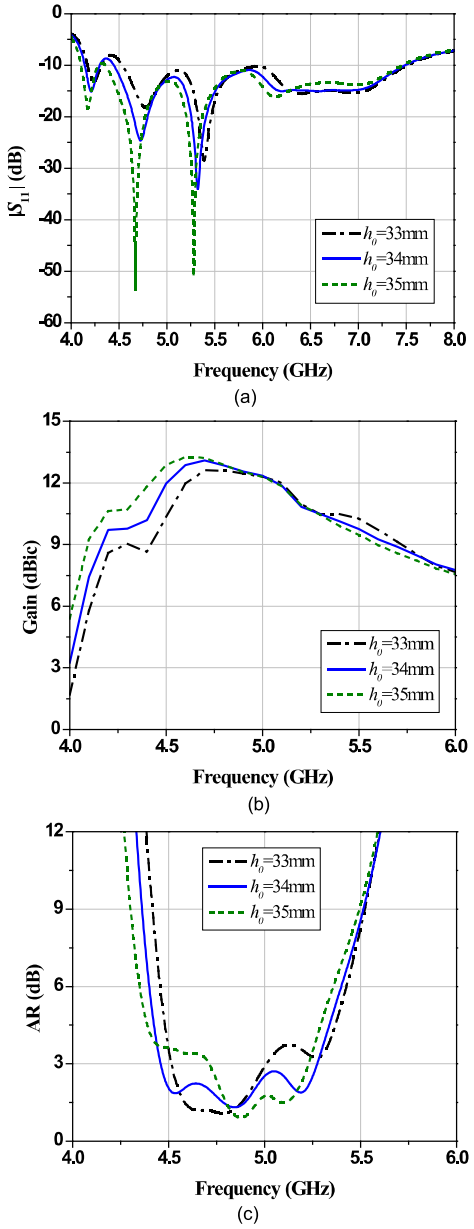

FIGURE 11. Simulated results of the Z-shaped MTS-based CP Fabry–Pérot antenna under variable h_0: (a) IBW, (b) gain, (c) ARBW.

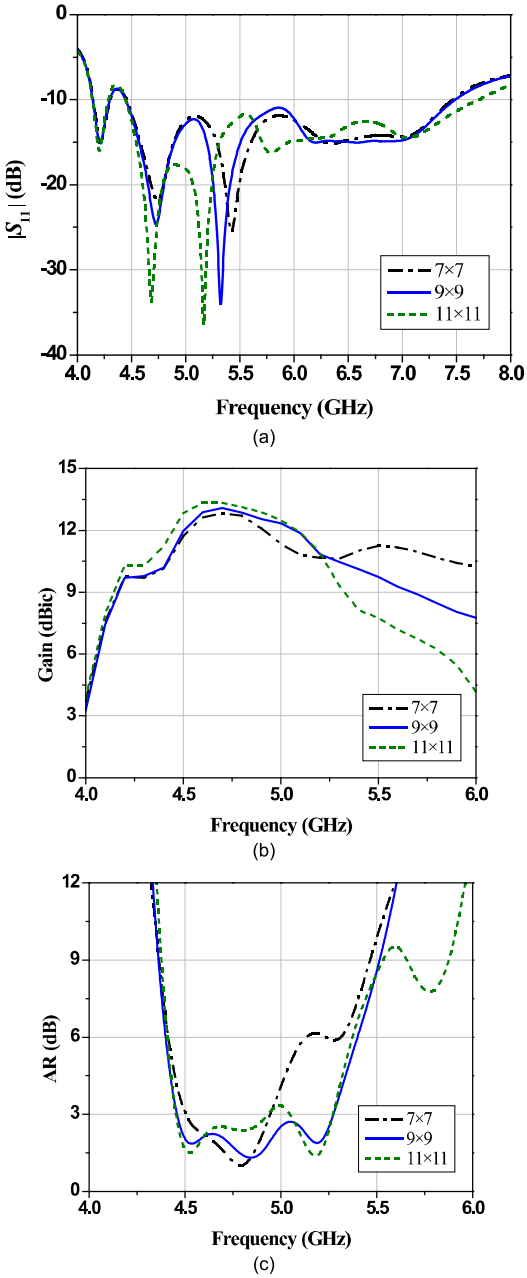

FIGURE 12. Simulated results of the Z-shaped MTS-based CP Fabry–Pérot antenna under variable the numbers of the Z-shaped MTS unit cells: (a) IBW, (b) gain, (c) ARBW.

IBW between 6 – 7 GHz. With $N = 11$ (31.62°), the resonance mode 5 occurs at 7.5 GHz, resulting in wider IBW. In addition, given $N = 7$, the minimum AR of 1.63 dB is achieved at 4.7 GHz with the resonance mode 2. With $N = 9$, the AR of 1.27 dB and 1.27 dB are achieved at 4.5 (resonance mode 2) and 5.2 GHz (resonance mode 3), respectively, giving rise to improved AR. With $N = 11$, the minimum AR of 0.63 dB is achieved at 5.2 GHz with the

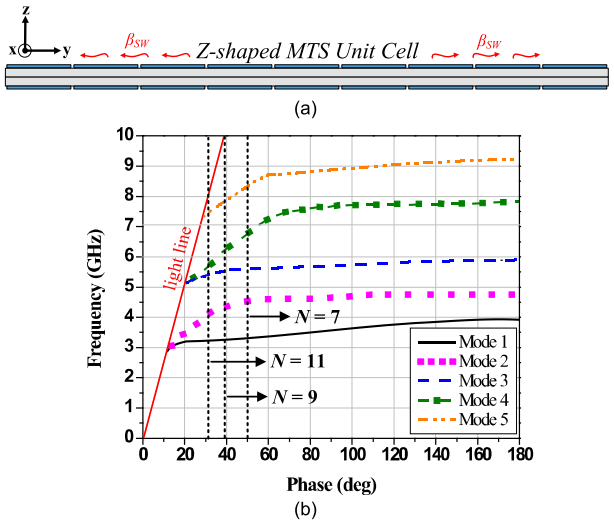

FIGURE 13. Simulation of the Z-shaped MTS unit cell: (a) surface wave resonance, (b) dispersion diagram.

resonance mode 3. However, with $N = 11$, ARBW at 5 GHz is greater than 3 dB due to the absence of resonance.

In Figure 14(a), the equivalent circuit diagram of the Z-shaped MTS unit cell [35] consists of an inductor (L_{M1}), series capacitors (C_{M1} and C_{M2}), parallel capacitor (C_{M3}), series inductor (L_{M2}), and series capacitor (C_{M4}), representing a Z-shaped element, the voids between any pair of Z-shaped elements, the coupling between the Z-shaped element and the square-shaped ground plane, the square-shaped ground plane, and the voids between any pair of square-shaped ground plane elements, respectively.

In Figure 14(b), the equivalent circuit diagram of the corners-truncated square patch consists [36] of an inductor (L_P) and parallel capacitor (C_P), representing the square patch with truncated corners. Meanwhile, the equivalent circuit diagram of the microstrip feed line with the H-shaped slot ground plane [37] consists of an inductor (L_F), parallel capacitor (C_{F1} and C_{F2}), inductor (L_{S1}), parallel capacitor (C_{S1}), parallel capacitor (C_{S2}), parallel inductor (L_{S2}), and resistance (R_S), representing the microstrip feed line and the H-shaped slot ground plane.

In Figure 14(c), the equivalent circuit diagram of the proposed Z-shaped MTS-based CP Fabry–Pérot antenna consists of the parallelly-connected equivalent circuits in Figures 14(a) and (b). The impedance of the Z-shaped MTS element with square-shaped ground plane (Z_1), the microstrip feed line (Z_2), H-shaped slot ground plane (Z_3), and corners-truncated square patch (Z_4) can be calculated by equations (9) – (12), respectively.

$$Z_1 = (C_{M1} + L_{M1} + C_{M2}) \parallel C_{M3} \parallel (L_{M2} + C_{M4}) = \left(\frac{j(\omega^2 L_{M1} C_{M1} C_{M2} - C_{M1} - C_{M2})}{\omega C_{M1} C_{M2}}\right) - (\omega C_{M3}/j) + \left(\frac{\omega C_{M4}}{j\omega^2 L_{M2} C_{M4} - j}\right) \quad (9)$$

TABLE 2. Optimal circuit components of the Z-shaped MTS-based CP Fabry–Pérot antenna.

Elements	L_{M1} (nH)	C_{M1} (pF)	C_{M2} (pF)	C_{M3} (pF)	L_{M2} (nH)	C_{M4} (pF)	L_P (nH)	C_P (pF)
Values (mm)	0.6	3.6	6.7	1.58	1.68	1.36	1	1.4
Elements	C_{F1} (pF)	C_{F2} (pF)	C_{S1} (pF)	L_F (nH)	L_{S1} (nH)	R_S (Ω)	C_{S2} (pF)	L_{S2} (nH)
Values (mm)	0.82	1.35	0.37	0.9	1	52	0.77	73

$$Z_2 = C_{F1} \parallel L_F \parallel C_{F2} = \frac{-j\left(L_F/\omega C_{F1} C_{F2}\right)}{j\omega L_F + 1/j\omega\left(1/C_{F1} + 1/C_{F2}\right)} \quad (10)$$

$$Z_3 = (L_{S1} \parallel C_{S1} \parallel C_{S2} \parallel L_{S2}) + R_S = j\omega(C_{S1} + C_{S2}) - j\left(\frac{L_{S2} - \omega L_{S1}}{\omega L_{S1} L_{S2}}\right) + R_S \quad (11)$$

$$Z_4 = L_P \parallel C_P = \frac{j\omega L_P}{1 - \omega^2 L_P C_P} \quad (12)$$

Advanced Design System (ADS) simulation is used to optimize the circuit components (R, L, C) of the equivalent circuit of the proposed Z-shaped MTS-based CP Fabry–Pérot antenna. Table 2 tabulates the optimal circuit components of the Z-shaped MTS-based CP Fabry–Pérot antenna.

Figure 15 compares the simulated IBW of CST and ADS simulation programs, and the simulation results are in good agreement. The lowest resonance frequencies ($|S_{11}| \leq -10$ dB) using CST simulation occur at 4.72 and 5.32, while those associated with ADS simulation are at 4.75 GHz and 5.43. CST simulation is used to optimize the antenna parameters that achieve very wide impedance bandwidth, while ADS simulation is utilized to verify the CST-generated optimal antenna parameters. Meanwhile, the equivalent circuit models are generated by ADS simulation and used to verify the CST simulation-generated optimal antenna parameters.

Figure 15 shows the equivalent circuit model to characterize the impedance matching [38] of the proposed antenna scheme. Figures 15(a)-(b) compares the simulated resistance, reactance, and IBW of the proposed antenna scheme using CST and ADS programs. The CST and ADS simulation results are in good agreement. The lowest resonance frequencies ($|S_{11}| \leq -10$ dB) using CST simulation occur at 4.72 and 5.32 GHz, while those associated with ADS simulation are at 4.75 and 5.43 GHz.

Figure 16 shows the surface current distribution with respect to phase variation (0°, 90°, 180°, and 270°) on certain sections of the Z-shaped MTS-based CP Fabry–Pérot antenna at 5 GHz (the center frequency). The direction of polarization of the proposed Z-shaped MTS-based CP Fabry–Pérot antenna can be observed by the rotation of the electric field along the propagation direction. The electric field vectors travel in the +z direction and rotate clockwise, giving rise to right-hand circular polarization (RHCP).

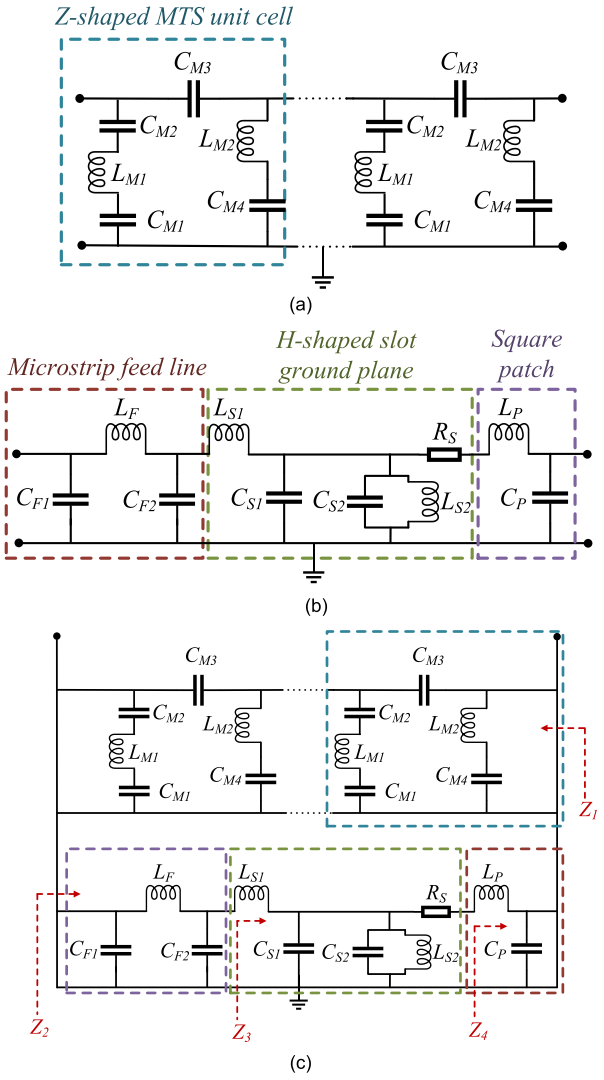

FIGURE 14. Equivalent circuit diagrams: (a) Z-shaped MTS unit cell, (b) source antenna, (c) the proposed Z-shaped MTS-based CP Fabry–Pérot antenna.

III. EXPERIMENTAL RESULTS

A Z-shaped MTS-based CP Fabry–Pérot antenna prototype was fabricated and experiments carried out. Figures 17(a)-(b) show the front and rear of the Z-shaped MTS-based CP Fabry–Pérot antenna prototype for C-band satellite communication system. Due to the fabrication limitations, the four Z-shaped MTS unit cells at the four corners of the upper substrate are deliberately removed and replaced with four holes in order to securely mount the three substrate layers together. The bolts and nuts to mount the three substrate layers are of polytetrafluoroethylene (PTFE) Teflon spacer, which has no effect on the antenna performance. In the antenna assembly, the distances between substrate layers are measured by a digital vernier caliper (500-196-30, Mitutoyo).

Figure 18 shows the measurement setup in an anechoic chamber using a vector network analyzer (Rohde&Schwarz ZNLE6 model). A pair of ETS-Lindgren Model 3102 Series Conical Log Spiral antennas (i.e., the transmitting antenna)

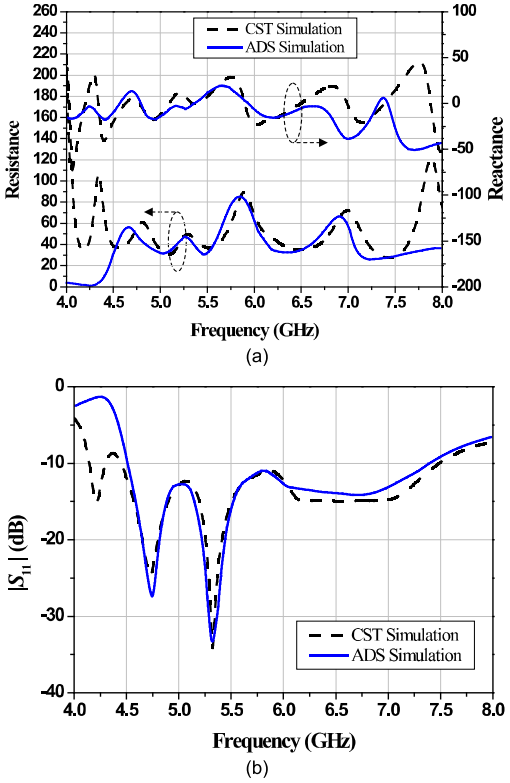

FIGURE 15. Comparison between the CST and ADS simulation: (a) resistance and reactance, (b) IBW.

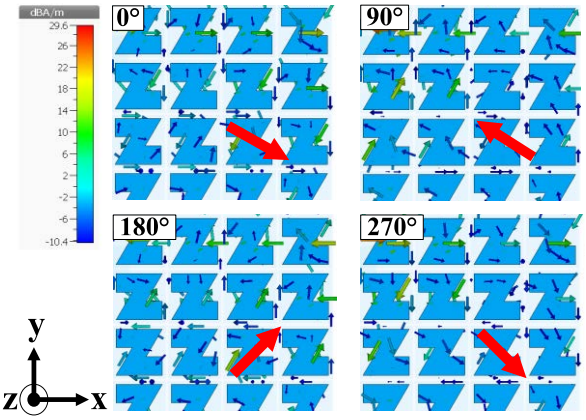

FIGURE 16. Surface current distribution of the Z-shaped MTS-based CP Fabry–Pérot antenna at 5 GHz.

are used to verify the right-hand (RHCP) and left-hand (LHCP) CP radiations of the prototype antenna (i.e., the receiving antenna). The far-field distance [39] between the transmitting and receiving antennas is 4 m. The experiments were carried out in two stages: first, calibrating the vector network analyzer using the calibration kit (ZV-Z235); and second, determining the performance of the prototype antenna.

The AR is determined by the co-polarization (co-pol) and cross-polarization (cross-pol) electric fields of the receiving antenna. The co-pol and cross-pol electric fields (E)

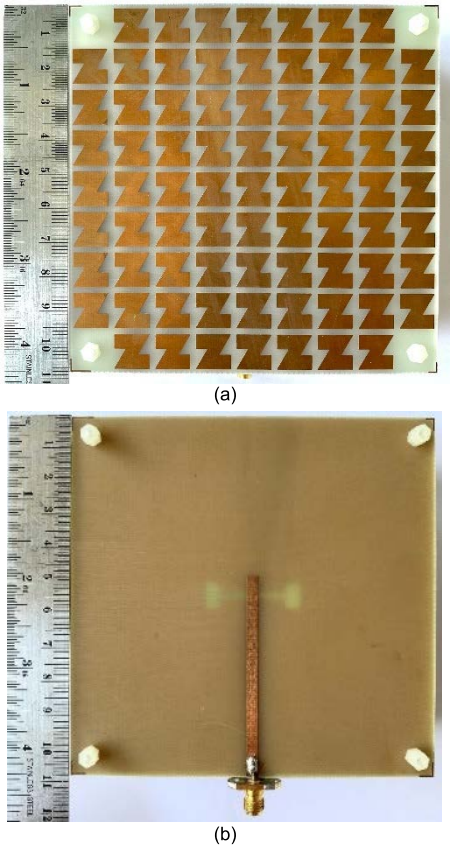

FIGURE 17. Prototype of the Z-shaped MTS-based CP Fabry–Pérot antenna: (a) front view, (b) rear view.

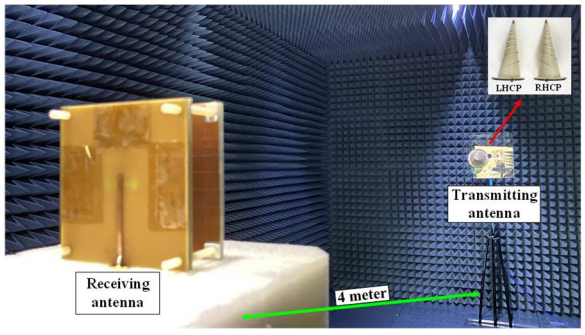

FIGURE 18. Measurement setup of the Z-shaped MTS-based CP Fabry–Pérot antenna.

between the transmitting and receiving antennas correspond to $|E_{co-pol}|$ and $|E_{cross-pol}|$. In other words, the co- and cross-pol electric fields correspond to RHCP and LHCP radiations, respectively. As shown in Figure 14, the radiation pattern of the proposed Z-shaped MTS-based CP Fabry–Pérot antenna is of RHCP. The AR can be calculated by equation (13) [40]

$$AR(\text{dB}) = 20\log\left(\frac{|E_{co-pol}| + |E_{cross-pol}|}{|E_{co-pol}| - |E_{cross-pol}|}\right) \quad (13)$$

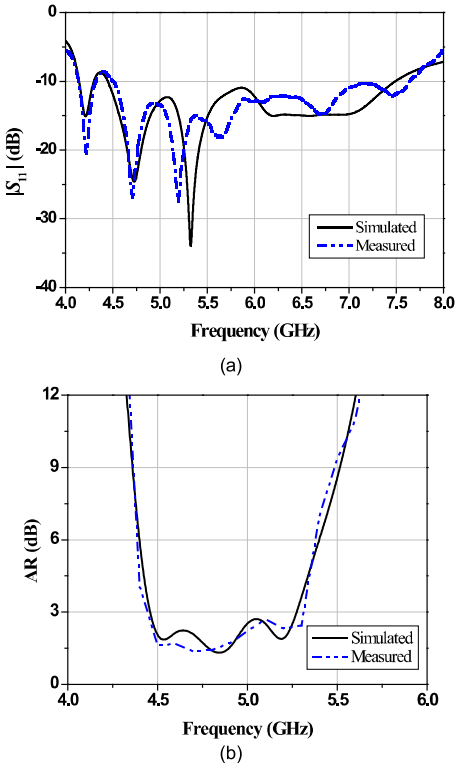

FIGURE 19. Simulated and measured results of the Z-shaped MTS-based CP Fabry–Pérot antenna: (a) IBW, (b) ARBW.

where $|E_{co-pol}|$ and $|E_{cross-pol}|$ are the electric field magnitudes of the co- and cross-pol between the transmitting and receiving antennas.

Figures 19(a)-(b) compare the simulated and measured IBW and ARBW of the Z-shaped MTS-based CP Fabry–Pérot antenna at the center frequency of 5 GHz. The simulated IBW ($|S_{11}| \leq -10$ dB) and ARBW (AR $\leq$ 3 dB) are 60% (4.4 – 7.4 GHz) and 16% (4.4 – 5.2 GHz), and the measured IBW and ARBW are 64% (4.4 – 7.6 GHz) and 18% (4.4 – 5.3 GHz). The simulated and measured results are agreeable.

In Figure 19(a), the simulated and measured IBW at the first (4.2 GHz) and second resonance (4.7 GHz) are in good agreement. Nonetheless, the measured IBW at the third resonance slightly shifts to the lower frequency (from 5.3 GHz to 5.2 GHz). The shift is attributable to the removal of the Z-shaped MTS unit cells at the four corners of the upper substrate to make room for the Teflon spacers to mount the three layers of substrate. The fourth resonance occurs at 5.6 – 5.75 GHz due to improved impedance matching. Essentially, the proposed Z-shaped MTS-based CP Fabry–Pérot antenna possesses very wide IBW, covering the frequency range of 4.4 – 7.6 GHz, resulting in the discarding of the first resonance.

Figures 20(a)-(c) show the simulated and measured RHCP and LHCP radiation patterns of the Z-shaped MTS-based CP Fabry–Pérot antenna in the xz- and yz-planes at 4.5, 5, and 5.2 GHz, respectively. The simulated and measured RHCP

TABLE 3. Comparison between existing CP MTS-based Fabry–Pérot antennas and the proposed Z-shaped MTS-based wideband CP Fabry–Pérot antenna.

References	f_0 (GHz)	IBW (%)	ARBW (%)	Maximum gain (dBic)	Feed Technique	Electrical dimension
[10]	5.8	8.6	2.5	17.3	LP single-feed	$5.0\lambda_0 \times 5.0\lambda_0 \times 0.50\lambda_0$
[11]	8.5	20	7	14.6	LP single-feed	$1.7\lambda_0 \times 1.7\lambda_0 \times 0.60\lambda_0$
[13]	10	5.8	4	17.8	LP single-feed	$2.9\lambda_0 \times 2.9\lambda_0 \times 0.36\lambda_0$
[15]	10	2.8	5	13.4	CP dual-feed	$2.6\lambda_0 \times 2.6\lambda_0 \times 0.36\lambda_0$
[16]	10	33	11.6	12	LP single-feed	$2.2\lambda_0 \times 2.2\lambda_0 \times 0.37\lambda_0$
[17]	9	13.8	21	11.2	LP single-feed	$1.8\lambda_0 \times 1.8\lambda_0 \times 0.38\lambda_0$
This work	5	64	18	12.88	LP single-feed	$1.5\lambda_0 \times 1.5\lambda_0 \times 0.51\lambda_0$

Note: f_0 is the center frequency of the CP Fabry–Pérot antenna; and λ_0 is the free-space wavelength corresponding to the lowest operating frequency.

are in good agreement, while those of LHCP are satisfactorily agreeable.

Figure 21 compares the simulated and measured 3-dB boresight gain bandwidth and radiation efficiency of the Z-shaped MTS-based CP Fabry–Pérot antenna. The simulated and measured 3-dB boresight gain bandwidths are 20% (4.4 – 5.4 GHz) and 30% (4.3 – 5.8 GHz), respectively. The simulated and measured maximum gain are 13.08 dBic at 4.7 GHz and 12.88 dBic at 4.7 GHz. The measured radiation efficiency is more than 50% over the operating frequency (4.4 – 5.3 GHz) of the Z-shaped MTS-based CP Fabry–Pérot antenna. Besides, the enhanced measured 3-dB boresight gain bandwidths at 5.1 – 5.25 GHz and 5.6 – 5.75 GHz are attributable to the higher radiation efficiency (4.6 – 5.25 GHz) and to the improved impedance matching (5.6 – 5.75 GHz), respectively.

Table 3 compares the existing CP MTS-based Fabry–Pérot antennas and the proposed Z-shaped MTS-based wideband CP Fabry–Pérot antenna in terms of the IBW, 3-dB ARBW, maximum gain, feed technique, and electrical dimension.

In [11], the CP single-feed hexagonal-shaped patch using superstrate encounters narrow ARBW in spite of wide IBW and high gain. In [13], the Fabry–Pérot antenna with polarization conversion metasurface (PCM) achieves high gain but fails to significantly enhance IBW and ARBW. Furthermore, in [15], the high-gain CP dual-feed Fabry–Pérot antenna using PCM is restricted by very narrow IBW and ARBW. In [16], the Fabry–Pérot patch array antenna with Wilkinson power divider feed network using chessboard PCM suffers from narrow ARBW despite wide IBW and high gain. In addition, the Wilkinson power divider feed network requires resistors, making the feed network very complex. In [17], the 2×2 PCM slot antenna array using sequentially-rotated feed network achieves wide ARBW and high gain but suffers from narrow IBW.

The wider IBW of the proposed antenna scheme, vis-à-vis those of the existing PRS-based antennas (Table 3), could be attributed to the periodically arranged Z-shaped MTS unit cells. The MTS unit cells function as the superstrate with high reflectivity and low transmittivity, resulting in the broadband IBW and high gain. Besides, the Z-shaped MTS unit cells convert LP to CP wave radiation with wide ARBW. Moreover, the H-shaped slot on the ground plane of the source antenna enhances the IBW. Meanwhile,

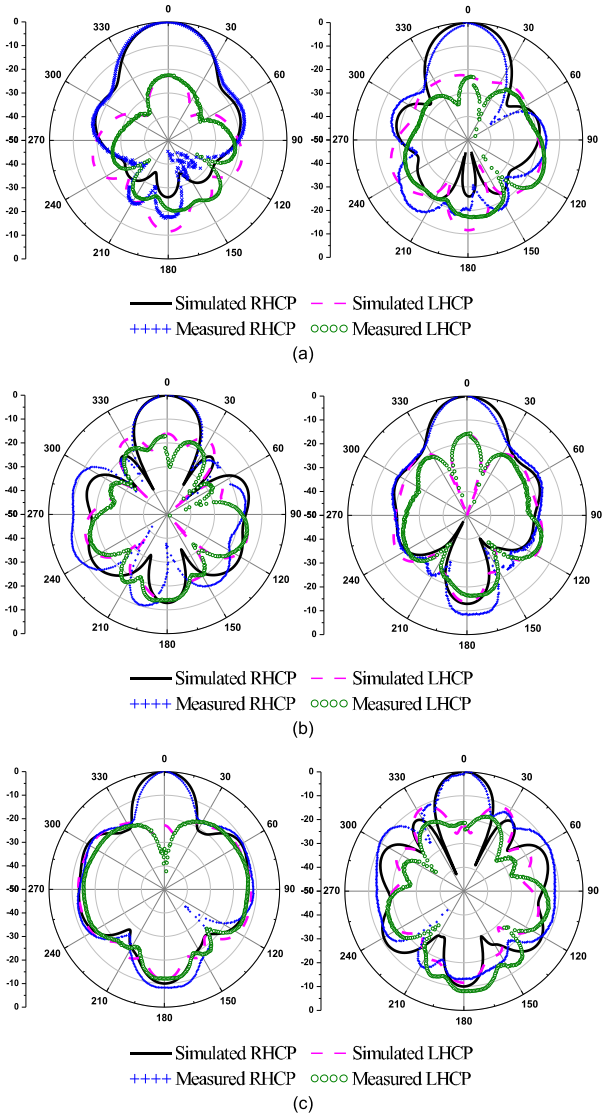

FIGURE 20. Simulated and measured RHCP (co-pol) and LHCP (cross-pol) radiation patterns at: (a) 4.5 GHz, (b) 5 GHz, (c) 5.2 GHz.

the proposed low-profile Z-shaped MTS-based CP Fabry–Pérot antenna for C-band frequency spectrum could achieve wide IBW and ARBW as well as high gain, rendering the proposed antenna scheme operationally ideal for satellite communication system.

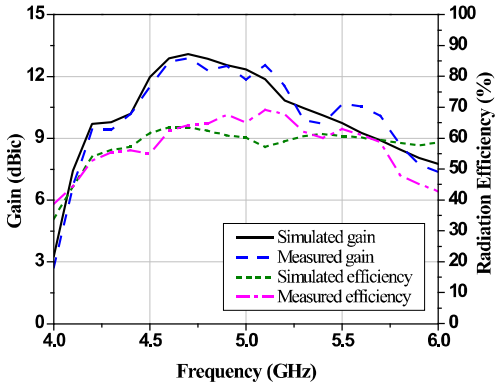

FIGURE 21. Simulated and measured 3-dB boresight gain bandwidth and radiation efficiency of the Z-shaped MTS-based CP Fabry–Pérot antenna.

IV. CONCLUSION

This research proposes a Z-shaped MTS-based wideband CP Fabry–Pérot antenna for C-band satellite communication. The proposed antenna is realized using three layers of FR-4 substrate (upper, middle, and lower) with air gaps between substrates. The upper substrate contains 9 × 9 periodically-arranged Z-shaped MTS unit cells, and at the center of the middle substrate sits the corners-truncated square patch. Meanwhile, the lower substrate consists of the H-shaped slot ground plane and the microstrip feed line. In the operation, the H-shaped slot ground plane with the microstrip feed line generates an LP wave which is subsequently radiated by the corners-truncated square patch. The Z-shaped MTS unit cells function as the partially reflective surface and LP-to-CP wave conversion, giving rise to high antenna gain and wide bandwidth.

The proposed Z-shaped MTS-based CP Fabry–Pérot antenna is initially modeled and simulated by using CST Studio Suite, and an antenna prototype was fabricated and experiments undertaken. The polarization conversion ratio (PCR) of the Z-shaped MTS unit cells is greater than 0.9, with a bandwidth of 23% (4.25 – 5.4 GHz) and normalized ellipticity of 1 (4.4 – 5.2 GHz) for RHCP. In addition, the CST- and ADS-simulated impedance matching ($|S_{11}| \leq -10$ dB) of the proposed antenna scheme are between 4.5 – 7.5 GHz. The measured IBW, ARBW, and 3-dB boresight gain bandwidth are 64% (4.4 – 7.6 GHz), 18% (4.4 – 5.3 GHz), and 30% (4.3 – 5.8 GHz). The measured maximum gain and radiation efficiency are 12.88 dBic at 4.7 GHz and over 50% in the frequency range of 4.4 – 5.3 GHz. The simulated and measured RHCP radiation patterns are in good agreement.

Due to low cost and light weight, compact satellites are increasingly adopted for low earth orbit (LEO) C-band satellite communication [41]. The compact satellites also require small antennas that are of low profile, low cost, high gain, wide IBW, and ARBW for transmitting and receiving signals to the ground station. The proposed low-profile Z-shaped MTS-based wideband CP Fabry–Pérot antenna for C-band frequency spectrum could achieve wide IBW and ARBW as well as high gain, rendering the proposed antenna scheme operationally suitable for satellite communication system.

REFERENCES

[1] N. Supreeyatitikul, D. Torrungrueng, and C. Phongcharoenpanich, "Quadri-cluster broadband circularly-polarized sequentially-rotated metasurface-based antenna array for C-band satellite communications," *IEEE Access*, vol. 9, pp. 67015–67027, 2021.

[2] K. X. Wang and H. Wong, "A circularly polarized antenna by using rotated-stair dielectric resonator," *IEEE Antennas Wireless Propag. Lett.*, vol. 14, pp. 787–790, 2015.

[3] Z.-G. Liu, Z.-X. Cao, and L.-N. Wu, "Compact low-profile circularly polarized Fabry–Perot resonator antenna fed by linearly polarized microstrip patch," *IEEE Antennas Wireless Propag. Lett.*, vol. 15, pp. 524–527, 2016.

[4] C. Chen, Z.-G. Liu, H. Wang, and Y. Guo, "Metamaterial-inspired self-polarizing dual-band dual-orthogonal circularly polarized Fabry–Pérot resonator antennas," *IEEE Trans. Antennas Propag.*, vol. 67, no. 2, pp. 1329–1334, Feb. 2019.

[5] P. Xie, G. Wang, X. Zou, and B. Zong, "Gain and AR improvements of the wideband circularly polarized Fabry–Perot resonator antenna," *IEEE Trans. Antennas Propag.*, vol. 69, no. 10, pp. 6965–6970, Oct. 2021.

[6] N. Hussain, M.-J. Jeong, J. Park, and N. Kim, "A broadband circularly polarized Fabry–Perot resonant antenna using a single-layered PRS for 5G MIMO applications," *IEEE Access*, vol. 7, pp. 42897–42907, 2019.

[7] R. Fakhte and I. Aryanian, "Compact Fabry–Perot antenna with wide 3 dB axial ratio bandwidth based on FSS and AMC structures," *IEEE Antennas Wireless Propag. Lett.*, vol. 19, no. 8, pp. 1326–1330, Aug. 2020.

[8] S. Zarbakhsh, M. Akbari, F. Samadi, and A. Sebak, "Broadband and high-gain circularly-polarized antenna with low RCS," *IEEE Trans. Antenn. Propag.*, vol. 67, no. 1, pp. 16–23, Jan. 2019.

[9] Y. Guan, Y.-C. Jiao, Y.-D. Yan, Y. Feng, Z. Weng, and J. Tian, "Wideband and compact Fabry–Perot resonator antenna using partially reflective surfaces with regular hexagonal unit," *IEEE Antennas Wireless Propag. Lett.*, vol. 20, no. 6, pp. 1048–1052, Jun. 2021.

[10] A. R. Vaidya, R. K. Gupta, S. K. Mishra, and J. Mukherjee, "Right-hand/left-hand circularly polarized high-gain antennas using partially reflective surfaces," *IEEE Antennas Wireless Propag. Lett.*, vol. 13, pp. 431–434, 2014.

[11] L. Leszkowska, M. Rzymowski, K. Nyka, and L. Kulas, "High-gain compact circularly polarized X-band superstrate antenna for CubeSat applications," *IEEE Antennas Wireless Propag. Lett.*, vol. 20, no. 11, pp. 2090–2094, Nov. 2021.

[12] J. Ren, W. Jiang, K. Zhang, and S. Gong, "A high-gain circularly polarized Fabry–Perot antenna with wideband low-RCS property," *IEEE Antennas Wireless Propag. Lett.*, vol. 17, no. 5, pp. 853–856, May 2018.

[13] P. Xie, G. Wang, H. Li, J. Liang, and X. Gao, "Circularly polarized Fabry–Pérot antenna employing a receiver-transmitter polarization conversion metasurface," *IEEE Trans. Antennas. Propag.*, vol. 68, no. 4, pp. 3213–3218, Apr. 2020.

[14] W. Cao, X. Lv, Q. Wang, Y. Zhao, and X. Yang, "Wideband circularly polarized Fabry–Perot resonator antenna in Ku-band," *IEEE Antennas Wireless Propag. Lett.*, vol. 18, no. 4, pp. 586–590, Apr. 2019.

[15] Y. Wang and A. Zhang, "Dual circularly polarized Fabry–Perot resonator antenna employing a polarization conversion metasurface," *IEEE Access*, vol. 9, pp. 44881–44887, 2021.

[16] Q. Chen and H. Zhang, "High-gain circularly polarized Fabry–Pérot patch array antenna with wideband low-radar-cross-section property," *IEEE Access*, vol. 7, pp. 8885–8889, 2019.

[17] K. Li, Y. Liu, Y. Jia, and Y. J. Guo, "A circularly polarized high-gain antenna with low RCS over a wideband using chessboard polarization conversion metasurfaces," *IEEE Trans. Antennas Propag.*, vol. 65, no. 8, pp. 4288–4292, Aug. 2017.

[18] Z.-G. Liu, W.-B. Lu, and W. Yang, "Enhanced bandwidth of high directive emission Fabry–Perot resonator antenna with tapered near-zero effective index using metasurface," *Sci. Rep.*, vol. 7, no. 1, pp. 1–10, Dec. 2017.

[19] Y. Sun, Z. N. Chen, Y. Zhang, H. Chen, and T. S. P. See, "Subwavelength substrate-integrated Fabry–Pérot cavity antennas using artificial magnetic conductor," *IEEE Trans. Antennas Propag.*, vol. 60, no. 1, pp. 30–35, Jan. 2012.

[20] A. P. Feresidis, G. Goussetis, S. Wang, and J. C. Vardaxoglou, "Artificial magnetic conductor surfaces and their application to low-profile high-gain planar antennas," *IEEE Trans. Antennas Propag.*, vol. 53, no. 1, pp. 209–215, Jan. 2005.
[21] I. Sohail, Y. Ranga, K. P. Esselle, and S. G. Hay, "A linear to circular polarization converter based on Jerusalem-cross frequency selective surface," in *Proc. 7th Eur. Conf. Antennas Propag. (EuCAP)*, Apr. 2013, pp. 2141–2143.
[22] H. Mirza, T. M. Hossain, P. J. Soh, M. F. Jamlos, M. N. Ramli, A. A. Al-Hadi, E. S. Hassan, and S. Yan, "Deployable linear-to-circular polarizer using PDMS based on unloaded and loaded circular FSS arrays for Pico-satellites," *IEEE Access*, vol. 7, pp. 2034–2041, 2019.
[23] P. Yang, R. Yang, and Y. Li, "Dual circularly polarized split beam generation by a metasurface sandwich-based Fabry–Pérot resonator antenna in Ku-band," *IEEE Antennas Wireless Propag. Lett.*, vol. 20, no. 6, pp. 933–937, Jun. 2021.
[24] Q. Zheng, C. Guo, and J. Ding, "Wideband and low RCS planar circularly polarized array based on polarization conversion of metasurface," *Microw. Opt. Techn. Lett.*, vol. 60, no. 3, pp. 784–789, Mar. 2018.
[25] T. Md Hossain, H. Mirza, P. J. Soh, M. F. Jamlos, R. A. Sheikh, A. A. Al-Hadi, and P. Akkaraekthalin, "Broadband single-layered, single-sided flexible linear-to-circular polarizer using square loop array for S-band pico-satellites," *IEEE Access*, vol. 7, pp. 149262–149272, 2019.
[26] H. Mirza, P. J. Soh, M. F. Jamlos, T. M. Hossain, M. N. Ramli, A. A. Al-Hadi, R. A. Sheikh, E. S. Hassan, and S. Yan, "A crossed dodecagonal deployable polarizer on textile and polydimethylsiloxane (PDMS) substrates," *Appl. Phys. A, Solids Surf.*, vol. 124, p. 178, Feb. 2018.
[27] L. Martinez-Lopez, J. Rodriguez-Cuevas, J. I. Martinez-Lopez, and A. E. Martynyuk, "A multilayer circular polarizer based on bisected split-ring frequency selective surfaces," *IEEE Antennas Wireless Propag. Lett.*, vol. 13, pp. 153–156, 2014.
[28] S. Yan and G. A. E. Vandenbosch, "Compact circular polarizer based on chiral twisted double split-ring resonator," *Appl. Phys. Lett.*, vol. 102, no. 10, Mar. 2013, Art. no. 103503.
[29] N. C. Karmakar and M. E. Bialkowski, "Circularly polarized aperture-coupled circular microstrip patch antennas for L-band applications," *IEEE Trans. Antennas Propag.*, vol. 47, no. 5, pp. 933–940, May 1999.
[30] V. Rathi, G. Kumar, and K. P. Ray, "Improved coupling for aperture coupled microstrip antennas," *IEEE Trans. Antennas Propag.*, vol. 44, no. 8, pp. 1196–1198, Aug. 1996.
[31] T.-H. Chang and J.-F. Kiang, "Compact multi-band H-shaped slot antenna," *IEEE Trans. Antennas Propag.*, vol. 61, no. 8, pp. 4345–4349, Aug. 2013.
[32] S.-X. Ta and I. Park, "Low-profile broadband circularly polarized patch antenna using metasurface," *IEEE Trans. Antennas Propag.*, vol. 63, no. 12, pp. 5929–5934, Dec. 2015.
[33] S. X. Ta and I. Park, "Artificial magnetic conductor-based circularly polarized crossed-dipole antennas: 2. AMC structure without grounding pins," *Radio Sci.*, vol. 52, p. 642, May 2017.
[34] *CST Microwave Studio Suite (User's Manual)*, CST Studio Suite (Reference Manual), Darmstadt, Germany, 2014.
[35] N. Supreeyatitikul, T. Lertwiriyaprapa, and C. Phongcharoenpanich, "S-shaped metasurface-based wideband circularly polarized patch antenna for C-band applications," *IEEE Access*, vol. 9, pp. 23944–23955, 2021.
[36] S. Verma and J. A. Ansari, "Analysis of U-slot loaded truncated corner rectangular microstrip patch antenna for broadband operation," *AEU Int. J. Electron. Commun.*, vol. 69, no. 10, pp. 1483–1488, Oct. 2015.
[37] K. Bangash, M. M. Ali, H. Maab, and R. A. Shaukat, "Effect of embedding H-Shaped slot on the characteristics of millimeter wave microstrip patch antenna for 5G applications," in *Proc. 2nd Int. Conf. Comput., Math. Eng. Technol. (iCoMET)*, Sukkur, Pakistan, Jan. 2019, pp. 1–4.
[38] P. Osklang, C. Phongcharoenpanich, and P. Akkaraekthalin, "Triband compact printed antenna for 2.4/3.5/5 GHz WLAN/WiMAX applications," *Int. J. Antennas Propag.*, vol. 2019, pp. 1–13, Aug. 2019.
[39] C. A. Balanis, *Antenna Theory: Analysis and Design*, 3rd ed. Hoboken, NJ, USA: Wiley, 2005.
[40] A. Sakonkanapong and C. Phongcharoenpanich, "Near-field HF-RFID and CMA-based circularly polarized far-field UHF-RFID integrated tag antenna," *Int. J. Antennas Propag.*, vol. 2020, pp. 1–15, Apr. 2020.
[41] S. Abulgasem, F. Tubbal, R. Raad, P. I. Theoharis, S. Lu, and S. Iranmanesh, "Antenna designs for CubeSats: A review," *IEEE Access*, vol. 9, pp. 45289–45324, 2021.

NATHAPAT SUPREEYATITIKUL received the B.Eng. degree from Mahidol University, Thailand, in 2014, the M.Eng. degree from the King Mongkut's University of Technology Thonburi (KMUTT), Thailand, in 2016, and the D.Eng. degree from the King Mongkut's Institute of Technology Ladkrabang (KMITL), Thailand, in 2022. His research interests include circularly polarized antennas and MIMO antennas.

AKKARAT BOONPOONGA (Member, IEEE) received the B.Eng. degree in electrical engineering from the King Mongkut's University of Technology North Bangkok (KMUTNB), Bangkok, Thailand in 2002, and the M.Eng. degree in telecommunications engineering and the D.Eng. degree in electrical engineering from the King Mongkut's Institute of Technology Ladkrabang (KMITL), Bangkok, in 2004 and 2008, respectively. He is currently an Associate Professor with the Department of Electrical and Computer Engineering, Faculty of Engineering, KMUTNB. His research interests include ground-penetrating radar (GPR), radar systems, radar target identification, the chipless RFID systems, and signal processing for EM applications. He is a member of the ECTI Association. He was a Board Committee Member of the ECTI Association, Thailand, from 2016 to 2017 and from 2020 to 2021.

CHUWONG PHONGCHAROENPANICH (Member, IEEE) received the B.Eng. (Hons.), M.Eng., and D.Eng. degrees from the King Mongkut's Institute of Technology Ladkrabang (KMITL), Bangkok, Thailand, in 1996, 1998, and 2001, respectively. He is currently a Professor with the Department of Telecommunications Engineering, KMITL, where he also works as the Leader of the Innovative Antenna and Electromagnetic Applications Research Laboratory. His research interests include antenna design for various mobile and wireless communications, conformal antennas, and array antenna theory. He is also a Senior Member of IEICE and a member of ECTI. He has served as the Chair for the IEEE MTT/AP/ED Thailand Chapter, from 2014 to 2018. He has been on Organizing Committee of several international conferences, including the TPC Chair of 2009 International Symposium on Antennas and Propagation (ISAP 2009) and a TPC Member of ISAP 2012. He is also a Reviewer of many scientific journals, including the IEEE TRANSACTIONS ON ANTENNAS AND PROPAGATION, IEEE ACCESS, *IET Microwaves, Antennas and Propagation*, *Electronics Letters*, and *ECTI Transactions*, and many international conferences, including ISAP and APMC. He was on the Board Committee of ECTI Association, from 2008 to 2011 and 2014 to 2015. He was an Associate Editor of the *IEICE Transactions on Communications* and the *ECTI Transactions on Electrical Engineering, Electronics, and Communications*. He is also an Associate Editor of the *IEICE Communications Express*.